Evolution of the pore size distribution in sheared binary glasses

Nikolai V. Priezjev[1] and Maxim A. Makeev[2]
[1]*Department of Mechanical and Materials Engineering, Wright State University, Dayton, Ohio 45435, USA*
[2]*Department of Chemistry, University of Missouri-Columbia, Columbia, Missouri 65211, USA*
(Received 24 August 2017; published 22 November 2017)

Molecular dynamics simulations are carried out to investigate mechanical properties and porous structure of binary glasses subjected to steady shear. The model vitreous systems were prepared via thermal quench at constant volume to a temperature well below the glass transition. The quiescent samples are characterized by a relatively narrow pore size distribution whose mean size is larger at lower glass densities. We find that in the linear regime of deformation, the shear modulus is a strong function of porosity, and the individual pores become slightly stretched while their structural topology remains unaffected. By contrast, with further increasing strain, the shear stress saturates to a density-dependent plateau value, which is accompanied by pore coalescence and a gradual development of a broader pore size distribution with a discrete set of peaks at large length scales.

DOI: 10.1103/PhysRevE.96.053004

I. INTRODUCTION

The design and synthesis of novel porous materials with advanced mechanical and thermal properties are important for various structural, environmental, and biomedical applications [1]. Therefore, a detailed understanding of the relationship between mechanical properties, including elastic and shear moduli, and porous structure of materials remains a major challenge. In the last two decades, a number of studies have numerically reconstructed the three-dimensional microstructure in silica and ceramic glasses [2,3] and metallic foams [4–6]. For example, it was recently demonstrated that during the initial stage of sintering of ceramic films the elastic modulus increases with the neck size of adjacent mono-size particles, while at the later stage of the coarsening process, the modulus becomes insensitive to details of the microstructure and only depends on porosity [3]. Moreover, the time evolution of the pore size distribution during the foaming process based on growth of pressurized pores was simulated using the data from two-dimensional metallographic images, and the resulting microstructure was used as an input for the finite element analysis of the stress-strain response of porous titanium [4].

In recent years, molecular dynamics (MD) simulations were used extensively to study the structure and mechanical properties of porous glassy materials [7–17]. In particular, it was shown that upon tensile loading, a periodic array of pores in metallic glasses causes strain localization along planes that contain pores and thus promotes the initialization and propagation of shear bands [11,16]. Interestingly, under large compressive deformation, the annihilation of adjacent pores can hinder propagation of shear bands and result in temporal hardening of porous metallic glasses [11]. Furthermore, it was found that in nanophase silica glasses, prepared by sintering at different pressures, the structure of pores is self-similar with the fractal dimension of about 2, and the short-range order is similar to bulk glasses, unlike the intermediate range order where the first sharp diffraction peak is smaller and shifted to smaller wave vectors [9]. The analysis of the MD data indicated that the elastic moduli of nanophase silica glasses scale with the density as $\sim\rho^{3.5}$ [9], while in the other MD study, the dependence of the elastic moduli on porosity in nanoporous silica was fitted by either exponential or power-law functions [13]. However, the exact relationship between the elastic, shear, and bulk moduli and the pore structure and size distribution in amorphous materials has not been established.

In the previous MD studies, the microtopography of binodal glassy systems at a low temperature was meticulously analyzed in quiescent samples of different densities [12,15,17]. Notably, it was found that the average pore size depends strongly on porosity, and the pore size distributions follow a universal scaling relation at small and intermediate length scales [17]. It was recently demonstrated that, under athermal quasistatic shear deformation, the structural evolution of porous glasses involves a formation of large voids, while the solid network fractures and becomes more compact with increasing strain until all atoms belong to a single large cluster [14]. Nevertheless, the time evolution of the porous network in sheared glassy solids at finite temperatures remains not fully understood.

In this paper, we study the dynamic response and evolution of three-dimensional porous structures in steadily sheared binary glasses using molecular dynamics simulations. The quiescent samples are produced via a coarsening process following a thermal quench across the glass transition at constant volume. It will be shown that with increasing shear strain, the individual pores become significantly deformed and in some cases connect with each other, leading to formation of large pores that are comparable with the system size. The results of molecular dynamics simulations indicate the power-law dependence of shear modulus on the average glass density.

The rest of the paper is organized as follows. The molecular dynamics simulation model, the glass preparation procedure, and the deformation protocol are described in the next section. The analysis of atom configurations and shear stress in quiescent and sheared porous glasses as well as the pore size distribution are presented in Sec. III. A summary of the results is given in the last section.

II. MOLECULAR DYNAMICS SIMULATIONS

We study a simple glass-forming system obtained via a deep quench at constant volume from a liquid state to a low temperature well below the glass transition [12,15,17]. During the coarsening process following the thermal quench,

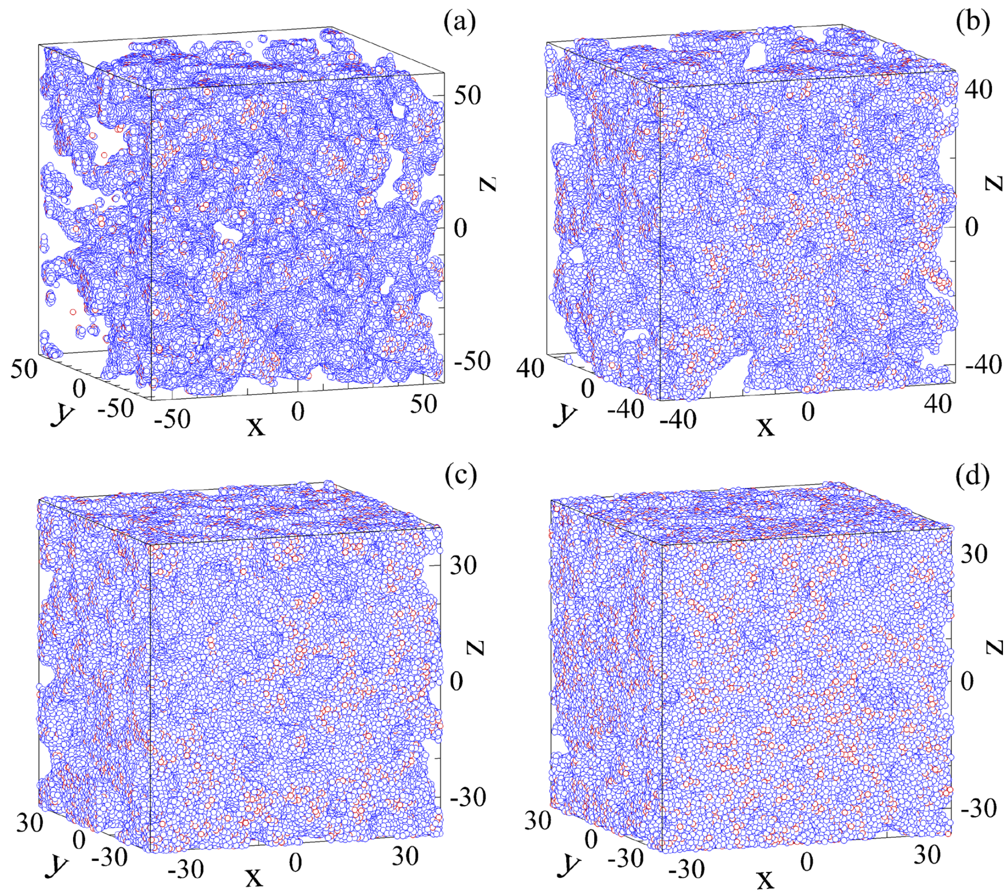

FIG. 1. Instantaneous atom configurations of the porous binary glass at the temperature $T = 0.05\,\varepsilon/k_B$ for the indicated average densities (a) $\rho\sigma^3 = 0.2$, (b) $\rho\sigma^3 = 0.4$, (c) $\rho\sigma^3 = 0.6$, and (d) $\rho\sigma^3 = 0.8$. Atoms of types A and B are denoted by blue and red circles, respectively. Note the different scales in all panels.

the system gradually evolves into a glassy state with porous structure, as shown in Fig. 1. In the binary (80:20) mixture model, the pairwise interaction between nearby atoms is described by the truncated Lennard-Jones (LJ)

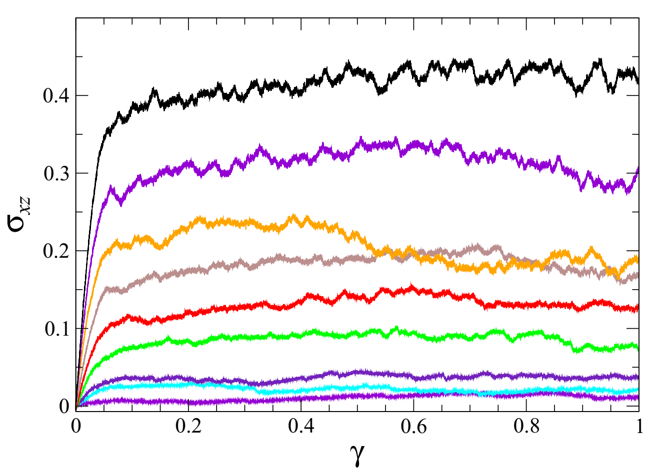

FIG. 2. The variation of shear stress σ_{xz} (in units of $\varepsilon\sigma^{-3}$) as a function of strain for the average glass densities $\rho\sigma^3 = 0.2$, 0.3, 0.4, 0.5, 0.6, 0.7, 0.8, 0.9, and 1.0 (from bottom to top). The shear rate is $\dot{\gamma} = 10^{-4}\,\tau^{-1}$ and temperature is $T = 0.05\,\varepsilon/k_B$.

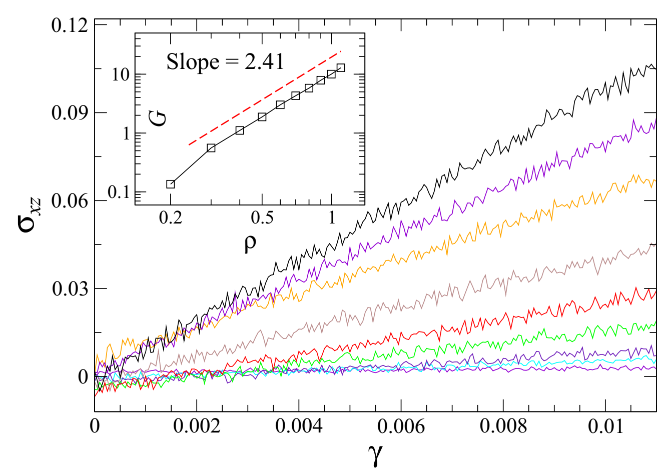

FIG. 3. The shear stress-strain curves at small strain $\gamma \lesssim 0.01$ and densities $\rho\sigma^3 = 0.2$, 0.3, 0.4, 0.5, 0.6, 0.7, 0.8, 0.9, and 1.0 (from bottom to top). The same data and color code as in Fig. 2. The inset shows the shear modulus G (in units of $\varepsilon\sigma^{-3}$) as a function of average glass density $\rho\sigma^{-3}$. The data were averaged over five independent samples. The red dashed line indicates the slope of 2.41.

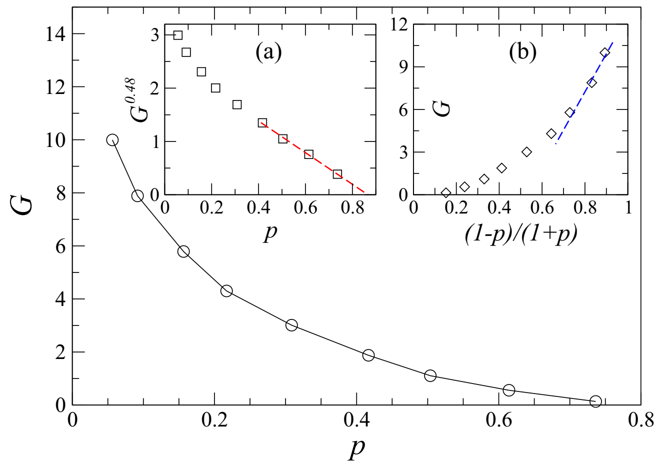

FIG. 4. The variation of shear modulus G (in units of $\varepsilon\sigma^{-3}$) as a function of porosity p. The inset (a) shows the same data plotted as $G^{0.48}$ vs p. The red dashed line is the best fit to the data for $p \gtrsim 0.4$. The inset (b) shows the dependence of G as a function of the variable $(1-p)/(1+p)$. The blue dashed line is a guide for the eye.

potential:

$$V_{\alpha\beta}(r) = 4\,\varepsilon_{\alpha\beta}\left[\left(\frac{\sigma_{\alpha\beta}}{r}\right)^{12} - \left(\frac{\sigma_{\alpha\beta}}{r}\right)^{6}\right], \tag{1}$$

with the interaction parameters $\varepsilon_{AA} = 1.0$, $\varepsilon_{AB} = 1.5$, $\varepsilon_{BB} = 0.5$, $\sigma_{AB} = 0.8$, $\sigma_{BB} = 0.88$, and $m_A = m_B$ [18]. Throughout the study, the cutoff radius is fixed at $r_{c,\alpha\beta} = 2.5\,\sigma_{\alpha\beta}$. All quantities are expressed in the LJ units where length, mass, energy, and time are measured in $\sigma = \sigma_{AA}$, $m = m_A$, $\varepsilon = \varepsilon_{AA}$, and $\tau = \sigma\sqrt{m/\varepsilon}$, respectively. The Newton's equations of motion were integrated using the velocity Verlet algorithm [19,20] with the time step $\triangle t_{\text{MD}} = 0.005\,\tau$.

Initially, the atoms were placed into a cubic box and the system was equilibrated at the high temperature of $1.5\,\varepsilon/k_B$, where k_B is the Boltzmann constant, during the time interval of $3\times 10^4\,\tau$ at constant volume. In the quiescent system, the temperature was regulated by simple velocity rescaling. It was previously shown that the critical temperature of the binary LJ model at $\rho\sigma^3 = 1.2$ is $T_c \approx 0.435\,\varepsilon/k_B$ [18]. In all our simulations, the total number of atoms of type A is $N_A = 240\,000$ and type B is $N_B = 60\,000$. The equilibration of the liquid phase was carried out in a wide range of densities $0.2 \leqslant \rho\sigma^3 \leqslant 1.0$ in five independent samples for each value of the glass density. After the equilibration procedure, the temperature was instantaneously reduced to the target temperature of $0.05\,\varepsilon/k_B$, and then the system was allowed to evolve at constant volume for an additional time interval of $10^4\,\tau$ to form a porous glass. Typical snapshots of atom configurations are presented in Fig. 1 for different average glass densities.

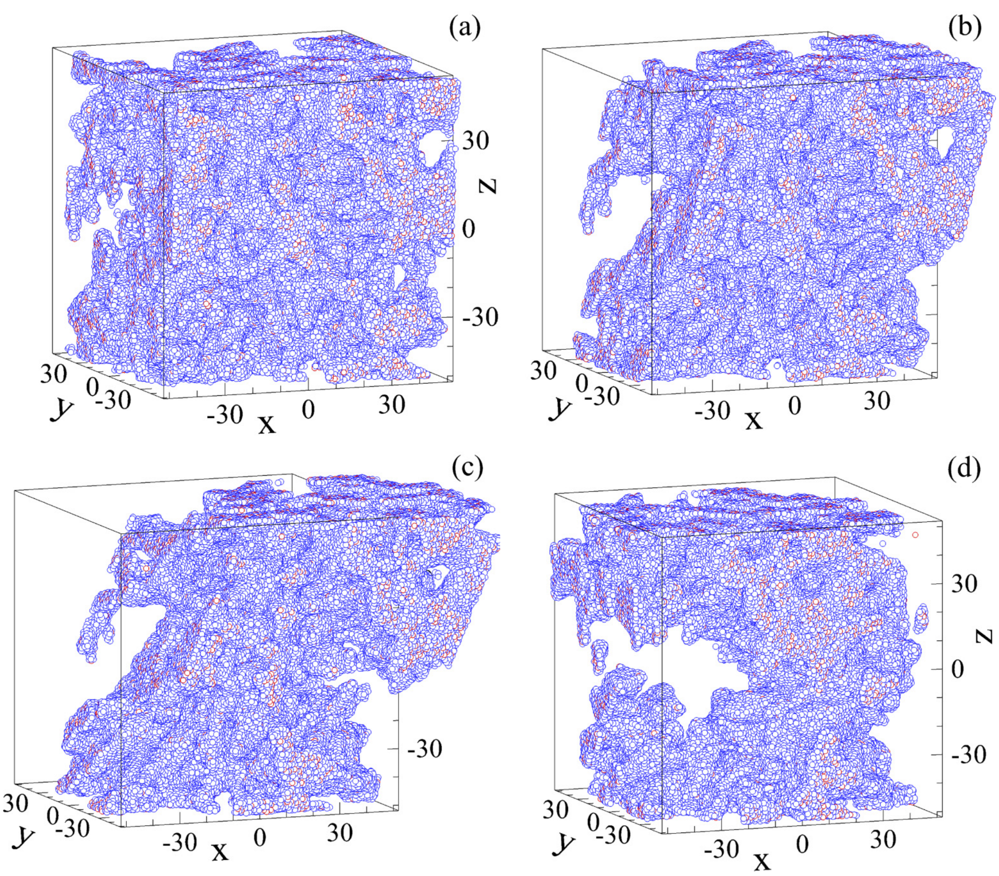

FIG. 5. A sequence of atom positions for the average glass density $\rho\sigma^3 = 0.3$ and shear strain (a) $\gamma = 0.05$, (b) $\gamma = 0.25$, (c) $\gamma = 0.45$, and (d) $\gamma = 0.95$. The strain rate is $10^{-4}\,\tau^{-1}$.

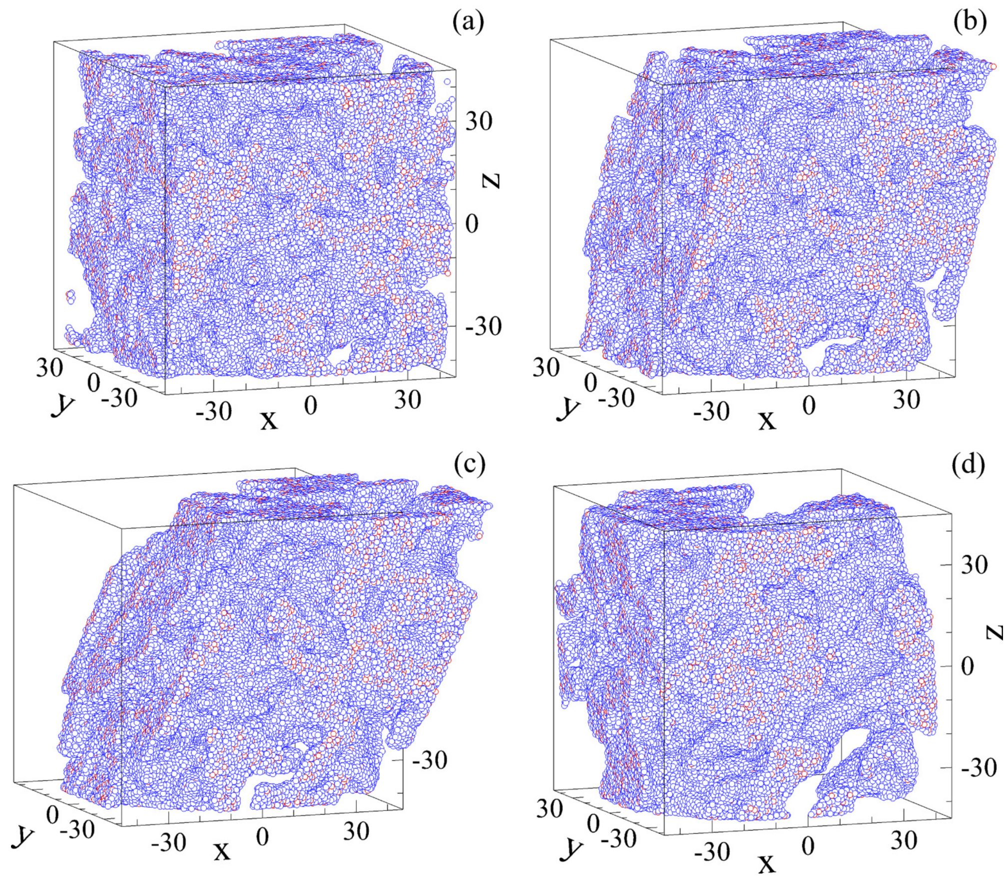

FIG. 6. Snapshots of atom positions for the average glass density $\rho\sigma^3 = 0.5$ and shear strain (a) $\gamma = 0.05$, (b) $\gamma = 0.25$, (c) $\gamma = 0.45$, and (d) $\gamma = 0.95$.

Next, the system was subjected to steady shear along the xz plane at a constant volume using the Lees-Edwards boundary conditions [21] with the strain rate of $10^{-4}\,\tau^{-1}$ during the time interval of $10^4\,\tau$. Thus, the maximum shear strain for all glass densities considered in the present study is 100%. In the deformation protocol, the temperature of $0.05\,\varepsilon/k_B$ was maintained by the Nosé-Hoover thermostat with the coupling parameter of 1.0 [19]. At the low temperature $T = 0.05\,\varepsilon/k_B$, a typical nonequilibrium simulation during $10^4\,\tau$ using 24 parallel processors required about 14 h. During the production run, the shear stress was computed every $0.5\,\tau$ and the positions of all atoms were saved every $500\,\tau$ and then used in the post-processing analysis of the pore size distribution and density profiles.

III. RESULTS

The formation of disordered porous structures during spinodal decomposition of a glass-forming liquid is influenced by a number of factors including the rate of thermal quench, target temperature, average density, and type of thermodynamic process [10]. While the binary system becomes fully demixed at either high temperatures or during slow quench, the separation kinetics is significantly slowed down after a fast quench to temperatures well below the glass transition, which leads to formation of structures with complex biphasic morphologies [12,15]. In the present study, the binary mixture was instantaneously brought from a high-temperature molten state to a glassy solid well below the glass transition. At a constant volume, the system slowly evolved towards the final structure with porous morphology that depends crucially on the average density. The representative atom configurations are displayed in Fig. 1 for the selected values of the average glass density $\rho\sigma^3 = 0.2$, 0.4, 0.6, and 0.8 at the temperature $T = 0.05\,\varepsilon/k_B$. It can be clearly seen that with decreasing glass density, the pores become larger and more interconnected. It was previously shown that the probability distribution of pore sizes in quiescent samples is well described by a Gaussian function at high densities, while as the average glass density decreases, the shape of distributions becomes asymmetrical and skewed toward larger length scales [17].

The dependence of shear stress as a function of strain in one sample is presented in Fig. 2 for different densities. As is evident, in all cases, the stress increases monotonically up to a few percent strain until it gradually reaches a quasiplateau and then decreases slightly at large strain. Note that the yield peak is absent in stress-strain curves even at higher densities, which is consistent with the results for sheared homogeneous glasses that were prepared by fast thermal quenching [22]. It can be observed from Fig. 2 that both the initial slope and the average value of the stress plateau become larger at higher glass densities. Notice, however, the presence of a significant deviation in shear stress from its average value at

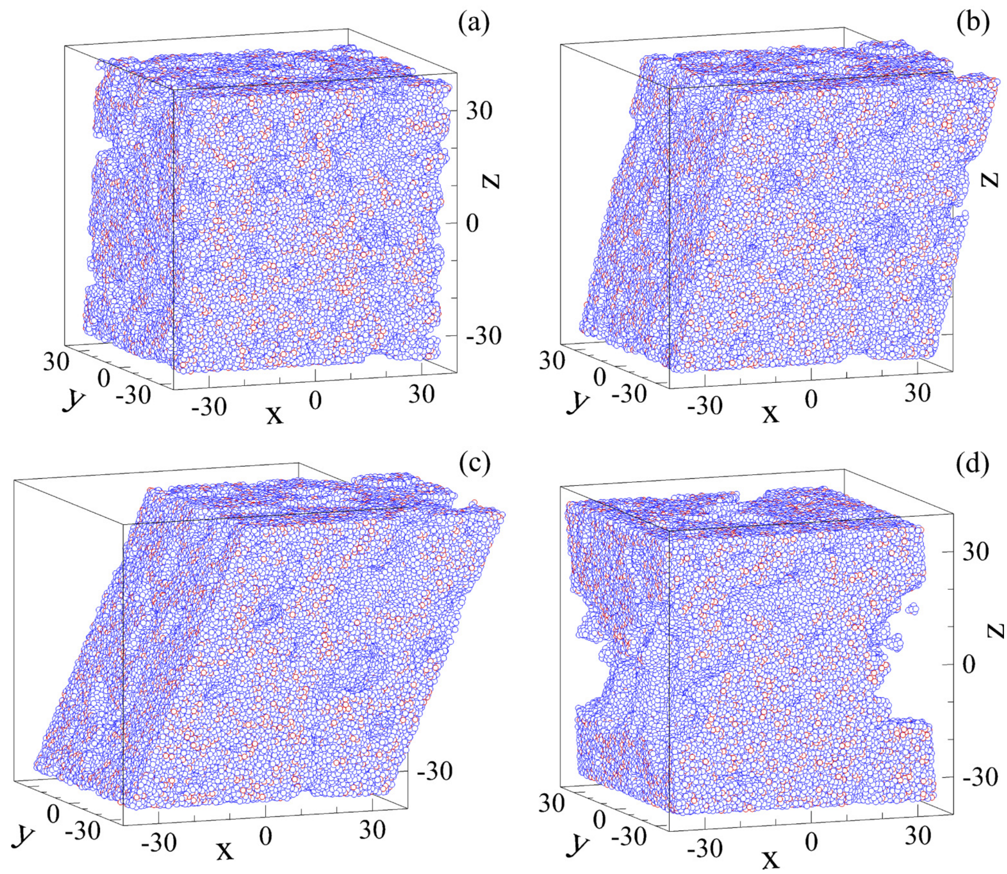

FIG. 7. Spatial configurations of atoms for the average glass density $\rho\sigma^3 = 0.8$ and strain (a) $\gamma = 0.05$, (b) $\gamma = 0.25$, (c) $\gamma = 0.45$, and (d) $\gamma = 0.95$. The same sample at zero strain is shown in Fig. 1(d).

large strain $\gamma \gtrsim 0.5$ for the case $\rho\sigma^3 = 0.8$, which is indicative of large shear-induced structural changes (discussed below). We further comment that results from test runs for very large shear strain deformation ($\gamma \lesssim 5$) showed pronounced stress oscillations with a typical period of about $10^4\,\tau$ (i.e., $\gamma = 1$), which implies that large solid domains can break up and unphysically reconnect via periodic boundary conditions. Therefore, in the present study, shear strain deformation only up to $\gamma \leqslant 1$ was considered.

An enlarged view of stress-strain curves at small values of strain, $\gamma \lesssim 0.01$, is displayed in Fig. 3 for the same set of densities as in Fig. 2. It is clearly seen that the shear stress increases linearly, with superimposed fluctuations, as a function of strain and the slope of the curves is larger at higher densities. We also find that at very small values of strain, $\gamma \lesssim 0.001$, the shear stress in some samples is slightly negative (see Fig. 3). The observed small deviation from zero stress in the absence of externally imposed strain appears as a result of the coarsening process where internal stresses become frozen in the porous structure [15,23]. Furthermore, in the inset to Fig. 3, the average shear modulus, which was computed from the linear slope of the stress-strain data at $\gamma \lesssim 0.01$, is shown as a function of the average glass density. As expected, the shear modulus strongly depends on the average density. The best fit to the MD data suggests the following scaling with the density: $G \sim \rho^{2.41}$. We also comment that test simulations at lower ($10^{-5}\,\tau^{-1}$) and higher ($10^{-3}\,\tau^{-1}$) strain rates have shown that, fluctuations aside, the stress-strain curves remain very similar to those plotted in Fig. 2 and the functional dependence of G versus the average glass density remains unchanged. Further insight can be gained by replotting the same data for the shear modulus as a function of porosity, as illustrated in Fig. 4.

In general, there exist two classes of models designed to describe the elastic properties of porous materials. The models belonging to the first class derive from the pioneering work by Eshelby on single ellipsoidal heterogeneity in an elastic medium [24]. Since the Eshelby's work, a considerable progress has been made to describe the mechanical response of heterogeneous systems. Several theoretical approaches, developed to date, specifically focus on the elastic moduli dependence on the volume fraction of voids, or the material's macro-porosity, p. The major approaches include, but are not limited to (1) the mean-field homogenization method [25,26], (2) the Mori-Tanaka model [27], (3) the generalized self-consistent model [28], and (4) the differential method [29]. It is not counterintuitive to hypothesize, however, that the above approaches (based on the Eshelby's tensors [24]) are good candidates for the problems dealing with ensembles of nonoverlapping inclusions; that is, at relatively low porosity, well above the percolation threshold, p_c. Note that the vast majority of experimental data available to date are obtained

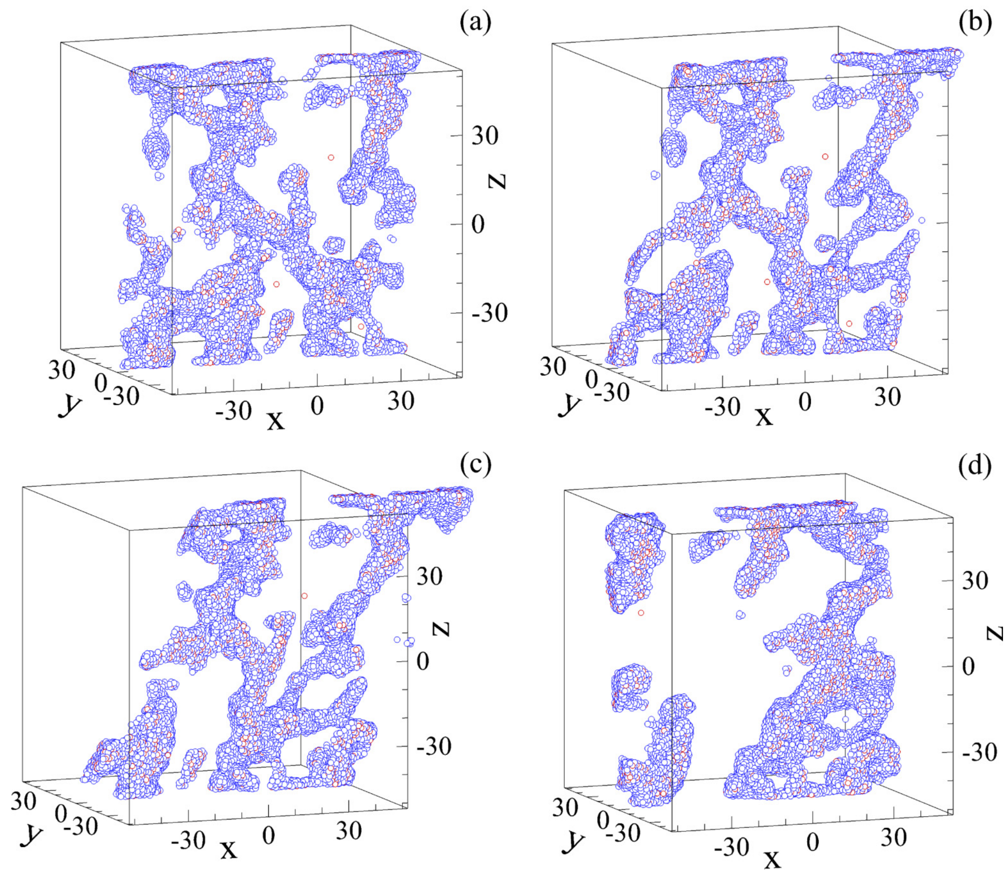

FIG. 8. A sequence of atom configurations within a slice of thickness 10σ for the average glass density $\rho\sigma^3 = 0.3$ and shear strain (a) $\gamma = 0.05$, (b) $\gamma = 0.25$, (c) $\gamma = 0.45$, and (d) $\gamma = 0.95$. The same data as in Fig. 5.

for porous materials with porosity below 0.5 (see, e.g., [30–33]). The highly porous systems may require a different approach. Indeed, the general topography of highly porous solids is characterized by length scales, which can be lower than the limits of applicability of the continuum elasticity theory. Moreover, the fractal properties of pores alone can introduce significant corrections to any continuum elasticity-based models.

The second class of models describing the elastic moduli in porous media is based on the concept of percolation. Correspondingly, in the frameworks of these models it is postulated that the elastic moduli dependence on porosity can be represented by the relation $E \sim (p_c - p)^f$, where E is the elastic modulus of the material. In three dimensions, the prediction of the percolation theory for the Young's modulus is $f = 2.1$ [34]. In the present study, we used both classes of models to fit our data; that is, we separate the regions of small porosity (ensemble of isolated inclusions in the elastic continuum; $p < 0.5$) and near-percolation-threshold network ($p > 0.5$). In the latter case, we used the following functional form for the shear modulus: $G = G_0\,(p_c - p)^f$. This approach leads to the following numerical values of the exponent and percolation threshold: $f = 2.1$ and $p_c = 0.87$ [see Fig. 4(a) inset]. In the former case, the dependence $G(p)$ at small values of porosity is best reproduced by the relation $G \sim (p-1)/(p+1)$, as shown in Fig. 4(b) inset. It should be emphasized, that the finite size of the systems under consideration can introduce some corrections to the aforedescribed behavior. However, we do not expect these corrections to be significant. As was shown in the past, the behavior follows $\sim L^{-1.14}$ relation [34], which is a minor effect for the system sizes we consider. One additional remark can be in order. As experimental studies have shown, the exponent for the elastic moduli can differ substantially from the theoretical predictions. For example, in Ref. [35], the reported value of the power-law exponent for aluminum foam is $f = 1.65$. Thus, further studies are of the essence.

The representative snapshots of atom configurations during steady shear deformation are shown in Figs. 5–7 for the average glass densities $\rho\sigma^3 = 0.3$, 0.5, and 0.8. To avoid a highly skewed simulation box, the configurations of atoms in the case $\gamma = 0.95$ are plotted within a tilted box with the strain $\gamma = -0.05$. From the consecutive snapshots, it can be observed that pores become significantly deformed and, with increasing shear strain, they tend to coalesce into larger voids. The deformation process of individual pores during strain loading can be more clearly visualized by plotting atom positions in a thin slice of 10σ along the plane of shear, as shown in Figs. 8–10. Generally, the formation of extended solid or void structures in a deformed glass is reflected in a large deviation of shear stress from its averaged value. For example, notice the appearance of a large pore in the center of

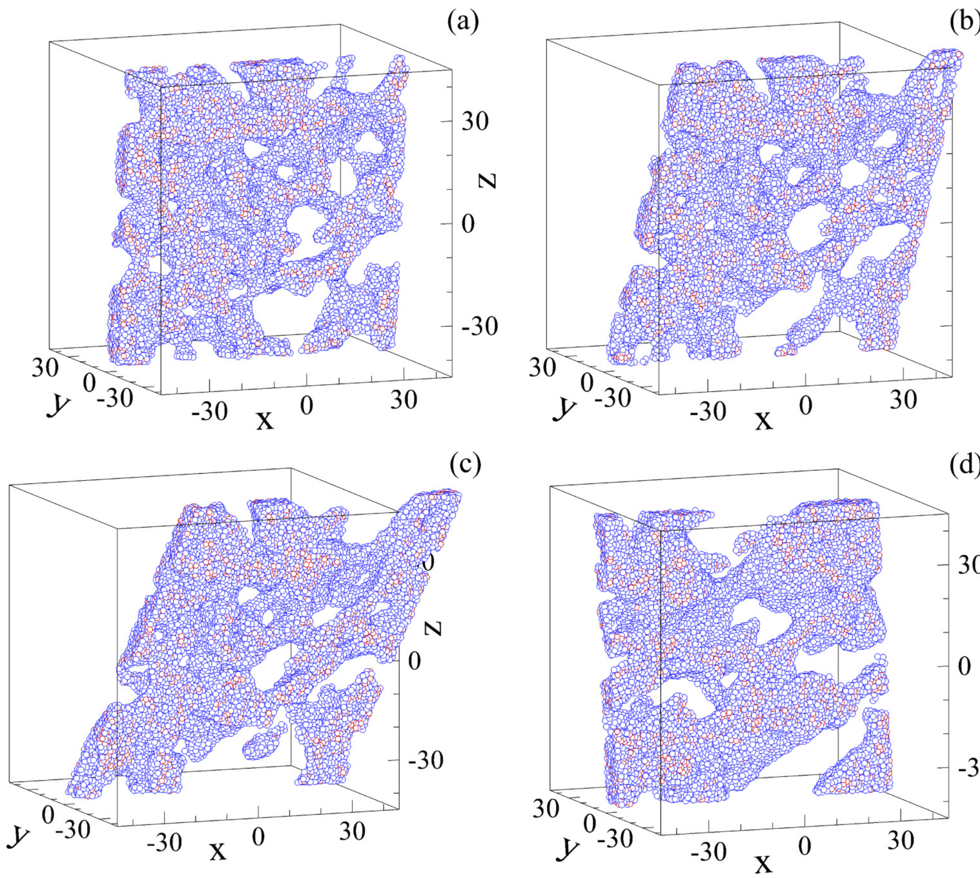

FIG. 9. Snapshots of the sheared system within the narrow slice of 10σ for the average glass density $\rho\sigma^3 = 0.5$ and shear strain (a) $\gamma = 0.05$, (b) $\gamma = 0.25$, (c) $\gamma = 0.45$, and (d) $\gamma = 0.95$. The same data as in Fig. 6.

the sample in Figs. 7(d) and 10(d) that correlates well with the reduced value of shear stress for $\gamma \gtrsim 0.5$ and $\rho\sigma^3 = 0.8$ in Fig. 2.

The position-dependent density profiles along the $\hat{z}$ direction are presented in Figs. 11, 12, and 13 for the average glass densities $\rho\sigma^3 = 0.3$, 0.5, and 0.8, respectively. In each case, the data were averaged in one sample at different strain values in thin slices parallel to the xy plane. It can be clearly observed that the local density in quiescent samples might be very different from the average bulk density. By definition, the local minima in density profiles correspond to one or more pores that are not necessarily connected with each other. Interestingly, it can also be noticed that with increasing shear strain, one of the local minima is further reduced. For example, the following regions become less dense: $25\sigma \lesssim z \lesssim 45\sigma$ in Fig. 8, $5\sigma \lesssim z \lesssim 20\sigma$ in Fig. 9, and $20\sigma \lesssim z \lesssim 45\sigma$ in Fig. 10. Thus, the shear-induced local expulsion of the solid phase suggests the formation of larger pores and flow localization in narrow regions. This behavior is consistent with the formation of shear bands running across the system in strained homogeneous amorphous materials [22,36–38].

In this study, the pore size distribution (PSD) functions were computed using the ZEO++ software tool [39,40]. Correspondingly, the analysis of pore size distributions, employed herein, is fully based on the algorithms and computational methods, described in Refs. [39,40]. In brief, the analysis is based on decomposition of each simulation system volume into Voronoi cells, associated with each individual atom in the atomic system under consideration. Thereby, a periodic Voronoi network is obtained for each system (note that periodic boundary conditions are applied in each case). The networks contain information on the nodes and edges of the Voronoi cells. The code tests whether the total volume of the systems is equal to the sum of the volumes of the computed Voronoi cells. Each node and edge is labeled with its distance to the corresponding set of nearest atoms. Thus, the obtained Voronoi network represents the void space in a porous material. By defining the probe radius, one can identify the probe-accessible regions of the Voronoi network. The implementation of the method, used to identify probe-accessible domains, is based on a variation of the Dijkstra's shortest-path algorithm [41]. The PSDs are computed using a probe radius of 1.2σ.

The pore size distribution functions, $\Phi(d_p)$, for sheared samples with densities $\rho\sigma^3 = 0.3$, 0.5, and 0.8 are presented in Figs. 14, 15, and 16, respectively. In agreement with the previous MD study [17], the distribution of pore sizes in quiescent samples is narrow at high glass densities and it becomes broader as the average glass density decreases. Under small shear deformation, $\gamma = 0.05$, the shape of PSD curves remains largely unaffected, indicating that pores are only slightly deformed under shear but do not coalesce. With further increasing strain, the distribution functions are progressively skewed toward large values of

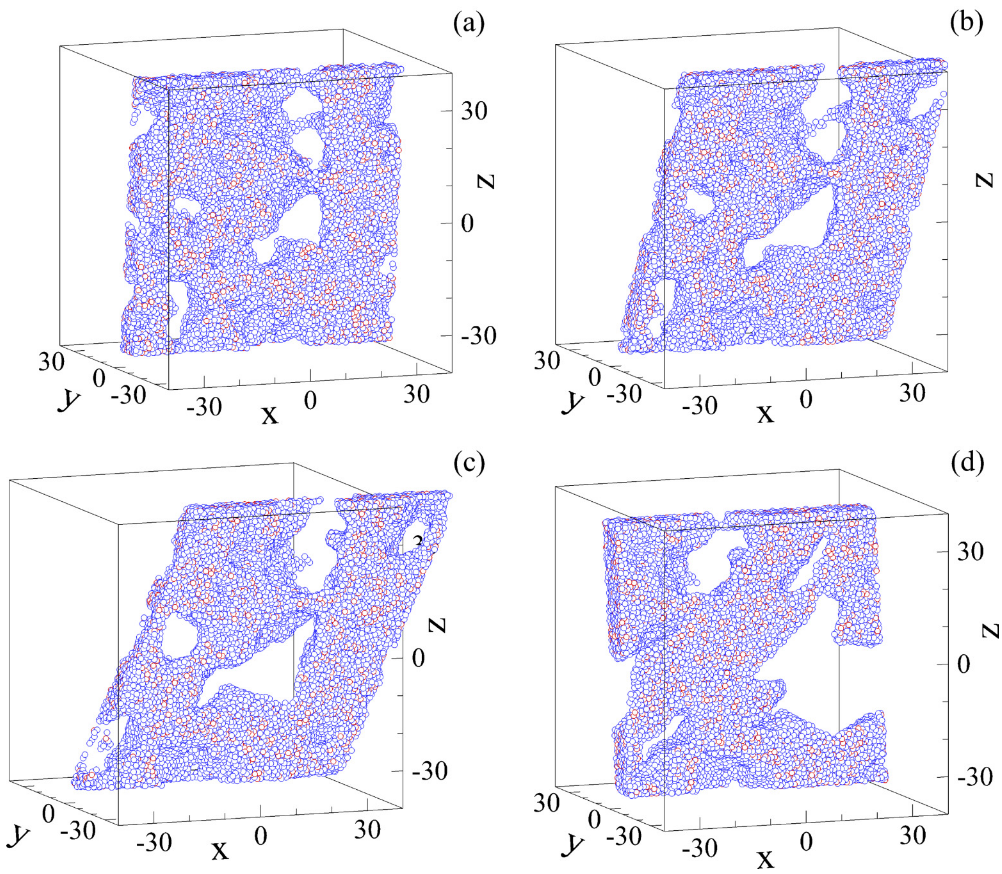

FIG. 10. Spatial configurations of atoms in a thin slice of $10\,\sigma$ for the average glass density $\rho\sigma^3 = 0.8$ and strain (a) $\gamma = 0.05$, (b) $\gamma = 0.25$, (c) $\gamma = 0.45$, and (d) $\gamma = 0.95$. The same sample at zero strain is shown in Fig. 1 (d). The same data as in Fig. 7.

d_p, and a number of discrete peaks are developed at large length scales. Note that the pronounced peaks in PSDs at large length scales, for example, at $d_p \approx 43.4\,\sigma$ for $\gamma = 0.90$ in Fig. 14, signify the appearance of elongated ("ellipsoid-like") porous structures with the typical smallest size of about d_p. In turn, the height of peaks reflects the number of attempts that were used to identify numerically the probe-accessible regions of the Voronoi network associated with large pores. We further comment that the largest length scale of elongated pores or the pore connectivity cannot be deduced from the PSD curves

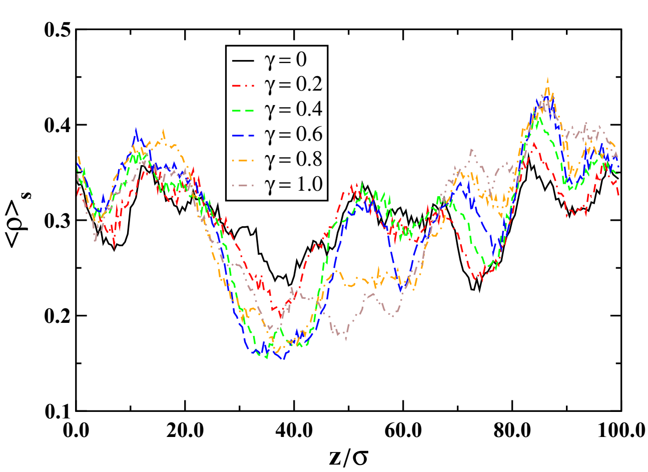

FIG. 11. The density profiles $\langle\rho\rangle_s$ (in units of σ^{-3}) along the $\hat{z}$ direction for the indicated values of strain. The data were averaged in thin slices parallel to the xy plane. The average glass density is $\rho\sigma^3 = 0.3$.

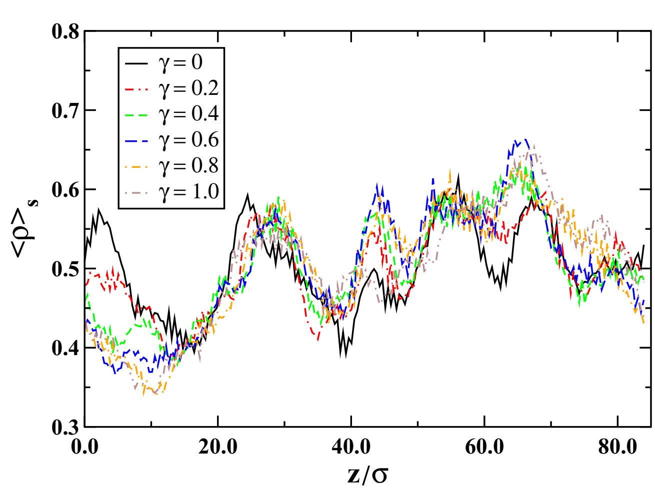

FIG. 12. The averaged density profiles $\langle\rho\rangle_s(z)$ (in units of σ^{-3}) for the selected values of shear strain. The average glass density is $\rho\sigma^3 = 0.5$.

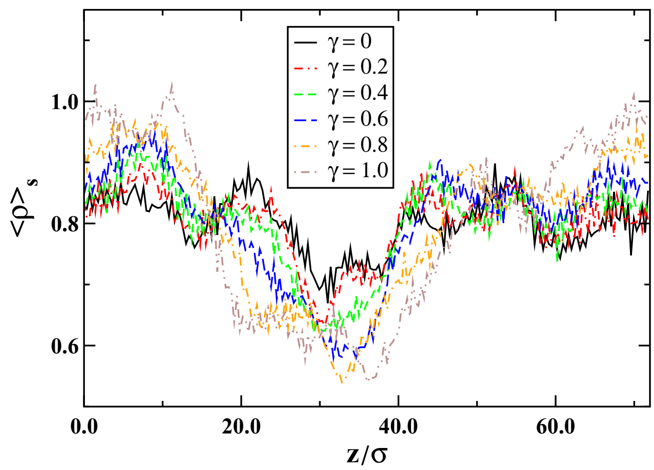

FIG. 13. The atomic density profiles $\langle\rho\rangle_s(z)$ (in units of σ^{-3}) as a function of shear strain. The average glass density is $\rho\sigma^3 = 0.8$.

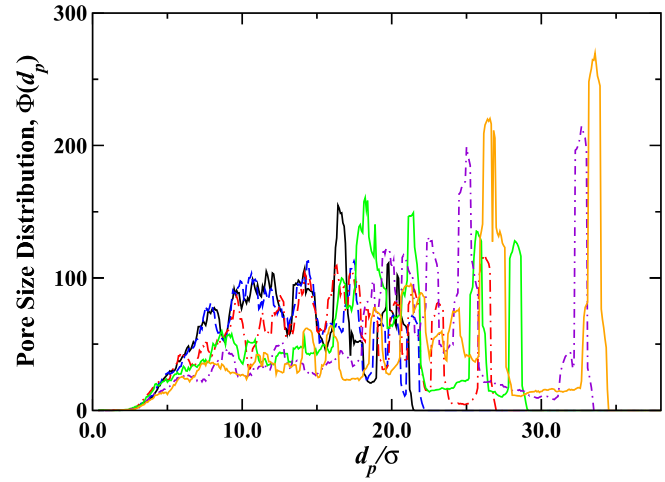

FIG. 15. The pore size distribution for the density $\rho\sigma^3 = 0.5$ and shear strain $\gamma = 0.0$ (black solid curve), 0.05 (blue dashed curve), 0.25 (red dash-dotted curve), 0.45 (green solid curve), 0.75 (velvet dash-dotted curve), and 0.90 (orange solid curve).

presented in Figs. 14–16. Altogether, it can be concluded that shear deformation is accompanied with a structural transition from a number of compact pores to a configuration with one or two dominant pores. This interpretation is consistent with the visual inspection of deformed samples presented in Figs. 5–7, where the formation of large pores is evident at large strain.

IV. CONCLUSIONS

In summary, molecular dynamics simulations were performed to examine mechanical properties and structural morphology of porous glasses under steady shear. We considered the three-dimensional binary mixture that was quenched at constant volume from a high-temperature liquid phase to a temperature well below glass transition. The coarsening process involved formation of disordered structures that were characterized by a relatively narrow pore size distribution with the largest length scale that depends on the average glass density. It was found that at small shear strain, the pore network becomes linearly transformed while its connectivity remains unchanged. Moreover, the dependence of shear modulus on porosity at low glass densities agrees well with continuum predictions based on the percolation theory. A strikingly different behavior occurs at large strain when the pore shape becomes extremely distorted and adjacent pores coalesce into large voids, which is reflected in the development of a skewed pore size distribution with a superimposed discrete peaks. Thus, the size of the largest pore is greater at lower average glass densities and higher shear strain.

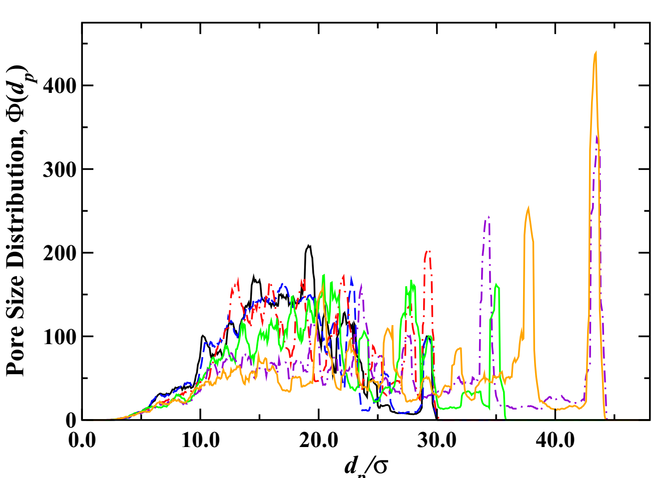

FIG. 14. The distribution of pore sizes for the average glass density $\rho\sigma^3 = 0.3$ and shear strain $\gamma = 0.0$ (black solid curve), 0.05 (blue dashed curve), 0.25 (red dash-dotted curve), 0.45 (green solid curve), 0.75 (velvet dash-dotted curve), and 0.90 (orange solid curve).

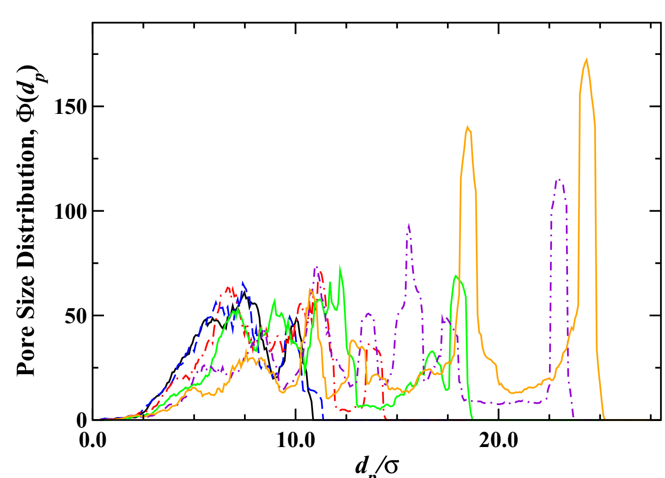

FIG. 16. The probability distribution of pore sizes for the average glass density $\rho\sigma^3 = 0.8$ and shear strain $\gamma = 0.0$ (black solid curve), 0.05 (blue dashed curve), 0.25 (red dash-dotted curve), 0.45 (green solid curve), 0.75 (velvet dash-dotted curve), and 0.90 (orange solid curve).

ACKNOWLEDGMENTS

Financial support from the National Science Foundation (Grant No. CNS-1531923) is gratefully acknowledged. The authors would like to thank Dr. M. Haranczyk (Lawrence Berkeley National Laboratory) for his help with the ZEO++ code. The molecular dynamics simulations were carried out using the LAMMPS numerical code developed at Sandia National Laboratories [19]. This work was supported in part by Michigan State University through computational resources provided by the Institute for Cyber-Enabled Research.

[1] X.-Y. Yang, L.-H. Chen, Y. Li, J. C. Rooke, C. Sanchez, and B.-L. Su, Hierarchically porous materials: Synthesis strategies and structure design, Chem. Soc. Rev. **46**, 481 (2017).

[2] L. D. Gelb and K. E. Gubbins, Pore size distributions in porous glasses: A computer simulation study, Langmuir **15**, 305 (1999).

[3] Z. Chen, X. Wang, F. Giuliani, and A. Atkinson, Microstructural characteristics and elastic modulus of porous solids, Acta Mater. **89**, 268 (2015).

[4] H. Shen, S. M. Oppenheimer, D. C. Dunand, and L. C. Brinson, Numerical modeling of pore size and distribution in foamed titanium, Mech. Mater. **38**, 933 (2006).

[5] R. Singh, P. D. Lee, T. C. Lindley, R. J. Dashwood, E. Ferrie, and T. Imwinkelried, Characterization of the structure and permeability of titanium foams for spinal fusion devices, Acta Biomater. **5**, 477 (2009).

[6] N. Michailidis, F. Stergioudi, H. Omar, and D. N. Tsipas, An image-based reconstruction of the 3D geometry of an Al open-cell foam and FEM modeling of the material response, Mech. Mater. **42**, 142 (2010).

[7] A. Nakano, L. Bi, R. K. Kalia, and P. Vashishta, Structural Correlations in Porous Silica: Molecular Dynamics Simulation on a Parallel Computer, Phys. Rev. Lett. **71**, 85 (1993).

[8] M. A. Makeev, M. A. Mazo, and E. F. Oleynik, in Physical and Chemical Methods of Investigation of Structure and Dynamics of Molecular Systems, Proceedings of the All-Russian Conference, June 27–July 2, Yoshkar-Ola, Russia, 1994, Vol. 2, pp. 41–44 (in Russian).

[9] T. Campbell, R. K. Kalia, A. Nakano, F. Shimojo, K. Tsuruta, P. Vashishta, and S. Ogata, Structural Correlations and Mechanical Behavior in Nanophase Silica Glasses, Phys. Rev. Lett. **82**, 4018 (1999).

[10] G. Foffi, C. De Michele, F. Sciortino, and P. Tartaglia, Arrested phase separation in a short-ranged attractive colloidal system: A numerical study, J. Chem. Phys. **122**, 224903 (2005).

[11] J. Wang, P. D. Hodgson, J. Zhang, W. Yan, and C. Yang, Effects of pores on shear bands in metallic glasses: A molecular dynamics study, Comput. Mater. Sci. **50**, 211 (2010).

[12] V. Testard, L. Berthier, and W. Kob, Influence of the Glass Transition on the Liquid-Gas Spinodal Decomposition, Phys. Rev. Lett. **106**, 125702 (2011).

[13] J. M. Rimsza and J. Du, Structural and mechanical properties of nanoporous silica, J. Am. Ceram. Soc. **97**, 772 (2014).

[14] L. Di Michele, D. Fiocco, F. Varrato, S. Sastry, E. Eisera, and G. Foffi, Aggregation dynamics, structure, and mechanical properties of bigels, Soft Matter **10**, 3633 (2014).

[15] V. Testard, L. Berthier, and W. Kob, Intermittent dynamics and logarithmic domain growth during the spinodal decomposition of a glass-forming liquid, J. Chem. Phys. **140**, 164502 (2014).

[16] D. Sopu, C. Soyarslan, B. Sarac, S. Bargmann, M. Stoica, and J. Eckert, Structure-property relationships in nanoporous metallic glasses, Acta Mater. **106**, 199 (2016).

[17] M. A. Makeev and N. V. Priezjev, Distributions of pore sizes and atomic densities in binary glasses revealed by molecular dynamics simulations, arXiv:1711.01689.

[18] W. Kob and H. C. Andersen, Testing mode-coupling theory for a supercooled binary Lennard-Jones mixture: The van Hove correlation function, Phys. Rev. E **51**, 4626 (1995).

[19] S. J. Plimpton, Fast parallel algorithms for short-range molecular dynamics, J. Comp. Phys. **117**, 1 (1995).

[20] M. P. Allen and D. J. Tildesley, *Computer Simulation of Liquids* (Clarendon, Oxford, 1987).

[21] D. J. Evans and G. P. Morriss, *Statistical Mechanics of Nonequilibrium Liquids* (Academic Press, London, 1990).

[22] Y. Shi and M. L. Falk, Strain Localization and Percolation of Stable Structure in Amorphous Solids, Phys. Rev. Lett. **95**, 095502 (2005).

[23] K. Maeda and S. Takeuchi, Atomistic process of plastic deformation in a model amorphous metal, Philos. Mag. A **44**, 643 (1981).

[24] J. D. Eshelby, The determination of the elastic field of an ellipsoidal inclusion, and related problems, Proc. R. Soc. London Ser. A **241**, 376 (1957).

[25] T. Mura, *Micromechanics of Defects in Solids* (Martinus Nijhoff Publishers, Leiden, 1987).

[26] R. M. Christensen, *Mechanics of Composite Materials* (Krieger Publishing Company, Malabar, 1991).

[27] T. Mori and K. Tanaka, Average stress in matrix and average elastic energy of materials with misfitting inclusions, Acta Mater. **21**, 571 (1973).

[28] R. M. Christensen and K. H. Lo, Solutions for effective shear properties in three phase sphere and cylinder models, J. Mech. Phys. Solids **27**, 315 (1979).

[29] R. Roscoe, The viscosity of suspensions of rigid spheres, Br. J. Appl. Phys. **3**, 267 (1952).

[30] S. Spinner, F. P. Knudsen, and L. Stone, Elastic constant-porosity relations for polycrystalline thoria, J. Res. Natl. Bur. Std. **67C**, 39 (1963).

[31] J. P. Panakkal, H. Willems, and W. Arnold, Nondestructive evaluation of elastic parameters of sintered iron powder compacts, J. Mater. Sci. **25**, 1397 (1990).

[32] J. C. Wang, Young's modulus of porous materials, J. Mater. Sci. **19**, 801 (1984); Part 2 Young's modulus of porous alumina with changing pore structure, **19**, 809 (1984).

[33] J. Coronel, J. P. Jernot, and F. Osterstock, Microstructure and mechanical properties of sintered glass, J. Mater. Sci. **25**, 4866 (1990).

[34] M. Sahimi, *Applications of Percolation Theory* (Taylor and Francis, London, 1994).

[35] J. Kováčik and F. Simancik, Aluminium foam – modulus of elasticity and electrical conductivity according to percolation theory, Scripta Mater. **39**, 239 (1998).

[36] V. Chikkadi, O. Gendelman, V. Ilyin, J. Ashwin, I. Procaccia, and C. A. B. Z. Shor, Spreading plastic failure as a mechanism for the shear modulus reduction in amorphous solids, Europhys. Lett. **110**, 48001 (2015).

[37] G. P. Shrivastav, P. Chaudhuri, and J. Horbach, Yielding of glass under shear: A directed percolation transition precedes shear-band formation, Phys. Rev. E **94**, 042605 (2016).

[38] N. V. Priezjev, Collective nonaffine displacements in amorphous materials during large-amplitude oscillatory shear, Phys. Rev. E **95**, 023002 (2017).

[39] R. L. Martin, B. Smit, and M. Haranczyk, Addressing challenges of identifying geometrically diverse sets of crystalline porous materials, J. Chem. Inf. Model. **52**, 308 (2012).

[40] T. F. Willems, C. H. Rycroft, M. Kazi, J. C. Meza, and M. Haranczyk, Algorithms and tools for high-throughput geometry-based analysis of crystalline porous materials, Micropor. Mesopor. Mater. **149**, 134 (2012).

[41] E. W. Dijkstra, A note on two problems in connexion with graphs, Numer. Math. **1**, 269 (1959).